CHEMISTRY OF MATERIALS

pubs.acs.org/cm

Article

Thermal Conditioning: An Effective and Inexpensive Strategy for Enhancing Ion Transport in Glass-Ceramics

Published as part of Chemistry of Materials special issue "Honoring the Outstanding Scientific Contributions of Clare Grey".

Islamiyat Ojelade,[‖] Erica Truong,[‖] Tej P. Poudel,[‖] Sawankumar Patel, Pawan K. Ojha, Yudan Chen, Ifeoluwa Oyekunle, Yongkang Jin, Md Mahinur Islam, Tehreem Toheed, Hannah Matos-Pimentel, Joey Peterson, and Yan-Yan Hu*

Cite This: *Chem. Mater.* 2026, 38, 3383−3391

Read Online

ACCESS | Metrics & More | Article Recommendations | Supporting Information

ABSTRACT: Slow cooling and heating cycles at relatively low temperatures (25 to 100 °C) are demonstrated to be an effective and practical strategy for improving ionic conductivity in oxyhalide, halide, and thiophosphate glass-ceramic electrolytes. In this study, Li_3PO_4−LiI, Li_3YBr_6, and Li_3PS_4 were chosen as the representative systems. Thermal conditioning improves Li^+-ion conduction by over 40%. Advanced characterizations using high-resolution NMR and XRD reveal four underlying mechanisms responsible for the increase in ionic conductivity, including the removal of low-conductivity impurities, the formation of high-conductivity phases, modification of the anion network, active cation redistribution, and enhanced ion mobility.

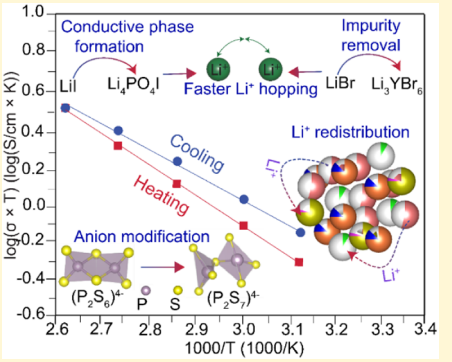

INTRODUCTION

Rechargeable lithium-ion batteries (LIBs) are widely used in portable electronic devices and electric vehicles.[1,2] All-solid-state batteries (ASSBs) employing solid electrolytes promise to improve safety and energy density beyond those of current-generation LIBs. Solid electrolytes offer several advantages over liquid electrolytes, including greater thermal and electrochemical stability, which enables different chemistry and higher energy density.[3,4] However, compared to liquid electrolytes, ion diffusion in solids is generally slower, which limits the power density of ASSBs.[5,6]

Previous studies have explored various strategies to enhance ionic conductivity in halide[7−9] thiophosphate[10,11] and oxyhalide solid electrolytes.[12,13] Yu et al. demonstrated that postsynthesis heat treatment of halide systems such as Li_3YBr_6 can significantly increase ionic conductivity by improving phase purity and lowering the activation energy for Li^+ migration.[14] For thiophosphate electrolytes such as Li_3PS_4, controlled heat treatment and partial crystallization of glassy precursors have been associated with enhanced ionic transport.[12,15] In mixed oxyhalide composites such as LiI−Li_3PO_4, Kaus and Ahmad showed that low-temperature sintering combined with compositional tuning improves conductivity relative to pure Li_3PO_4.[12,16] Although these approaches have proven effective, they often require high temperatures, extended processing times, or material-specific optimization,[14,17−25] limiting their general applicability and energy efficiency. Consequently, a broadly applicable, low-temperature, and cost-effective method for enhancing ion transport across multiple classes of solid electrolytes remains lacking. Thermal conditioning, achieved through heating and cooling cycles, is one of the most accessible tools for improving ionic conductivities in solids.[26,27] However, the effects of thermal conditioning on structures and ion dynamics are nontrivial and often elusive.

Understanding these effects not only enables us to employ thermal conditioning as an effective tool to accelerate ion migration but also helps us understand the changes that occur during battery cycling due to local heating. During battery charging and discharging, heat is generated by electrochemical reactions that cannot dissipate quickly, affecting the internal temperature distribution within the battery.[3,4,28] This, in turn, can lead to multiple issues, including aging of battery materials,[29] degradation at multiple interfaces,[30] stress

Received: November 18, 2025
Revised: March 11, 2026
Accepted: March 16, 2026
Published: March 19, 2026

https://doi.org/10.1021/acs.chemmater.5c03118
Chem. Mater. 2026, 38, 3383−3391

cracking,[31] and thermal runaway.[32] These various issues then degrade battery safety and lifespan. Therefore, understanding thermal effects is essential for developing long-lasting, high-performance ASSBs.

In this work, we investigated the thermal processes of three classes of solid electrolytes: halides, thiophosphates, and oxyhalides. We have demonstrated that short heating and cooling treatments within a moderate temperature range enhance ion transport in solid electrolytes. We dub this phenomenon "thermal conditioning" (TC). Thermal conditioning was performed between 25 and 100 °C to evaluate the effect of moderate to low-temperature treatment on ion transport. This temperature window was chosen to allow subtle changes in local structures and ion transport without inducing high-temperature annealing, providing a cost-effective and energy-efficient approach to enhance ionic conductivity. Electrochemical impedance spectroscopy (EIS) measurements indicate that the ionic conductivities of the three classes of materials increased by more than 40%. We employed solid-state nuclear magnetic resonance (NMR) and powder X-ray diffraction (P-XRD) to elucidate how the structures and ion dynamics of the solid electrolytes change with thermal conditioning. Thermal conditioning generally improves ion transport for the following reasons: (1) removal of low-conducting phases and generation of high-conducting phases, (2) modification of anion sublattices and creation of anion disorder conducive to fast ion transport, (3) redistribution of active cations, and (4) increased ion dynamics.

EXPERIMENTAL METHODS

Synthesis of Solid Electrolytes

Li_3PO_4−LiI electrolytes were synthesized following the methods reported by Patel et al.[13] Lithium iodide (99.9%, Alfa Aesar) and lithium phosphate (99%, Sigma-Aldrich) were mixed in a 1:1.4 molar ratio and hand-ground to a homogeneous powder using an agate mortar and pestle. The ground powder was then transferred to a 25 mL zirconia jar containing two 10 mm zirconia balls and mechanochemically milled for 20 h using a SPEX 8000M ball mill machine. Because the SPEX mill operates in continuous oscillatory mode, no milling cycles or rest intervals were applied; the sample was milled continuously for the full 20 h duration. The as-milled powder was then stored in an argon glovebox. Samples were cold-pressed into pellets using a 6 mm pellet mold die set at 250 psi for characterization.

Li_3YBr_6 electrolytes were synthesized following the methods reported by Poudel et al.[33] Lithium bromide (99.9% Sigma-Aldrich) was initially vacuum-dried dynamically at 200 °C for 12 h to remove moisture, then stored in an argon-filled glovebox. Anhydrous YBr_3 (99.9% purity, Thermo Scientific) was stored in the same argon-filled glovebox and used as received. Stoichiometric amounts of LiBr and YBr_3 were hand-ground using a mortar and pestle. The powder was then transferred into a quartz tube and covered with parafilm to prevent exposure to moisture. The quartz tube was promptly sealed with hydroxy flame under a dynamic vacuum. The sealed tube was heated to 600 °C at a rate of 2.4 °C min^{-1} and held at this temperature for 24 h. It was then cooled to 22 °C for an additional 24 h at a controlled rate of 0.4 °C min^{-1} to achieve crystallization. The as-prepared comelted sample was harvested from the quartz tube inside an argon-filled glovebox (MBraun) to avoid air exposure and hand-ground for 10 min. ∼66 mg of Li_3YBr_6 powder was pressed into 6 mm diameter pellets inside an Ar-filled glovebox using a stainless-steel mold under ∼300 psi. The remaining powder was stored in a glass vial for further characterization.

Li_3PS_4 electrolytes were prepared in an argon-filled environment. The precursors, Li_2S (99% Thermo Scientific) and P_2S_5 (99% Sigma-Aldrich), were weighed in stoichiometric proportions and hand-milled using an agate mortar and pestle. The resulting homogenized powder was transferred into a 25 mL zirconia jar containing two 10 mm zirconia balls, and the jar was vacuum-sealed. The sealed jar was then subjected to mechanochemical ball-milling for 20 h using SPEX 8000M ball-mill machine. ∼66 mg of the obtained sample was then pelletized using a 6 mm pellet mold under ∼500 psi in the argon-filled glovebox. The remaining sample was set aside for other analyses.

The batch size for all solid electrolyte preparations is 350−500 mg. Additionally, no external stack pressure was applied during impedance measurements. After the pellets were loaded into a 6 mm cylindrical cell, the electrodes were gently hand-tightened to ensure good electrical contact without causing mechanical damage to the pellets.

Electrochemical Measurements

The ionic conductivities of the electrolytes were determined using AC electrochemical impedance spectroscopy (EIS) acquired with a Gamry Analyzer Reference 600+ over a frequency range of 5 MHz to 1 Hz. Electrolyte pellets were placed into a custom-built cylindrical cell and sandwiched between indium foils as blocking electrodes.

The Thermal Conditioning process was performed under vacuum using a BioLogic electrochemical analyzer coupled to a CSZ MicroClimate Chamber. The sample was heated from 20 to 100 °C in 20 °C increments, with a 15 min dwell time at each temperature to ensure thermal equilibration. The heating and cooling followed the programmed chamber ramp rate of ∼2 °C min^{-1}. Electrochemical impedance spectra were collected over the frequency range 5 MHz−1 Hz with an applied AC amplitude of 10 mV. After reaching 100 °C, EIS measurements were recorded during the cooling cycle from 100 °C back to 20 °C in 20 °C increments, with a 15 min dwell at each step. Room-temperature ionic conductivities were collected before and after TC experiments.

Powder X-ray Diffraction

Powder X-ray diffraction (PXRD) was performed using a Rigaku D8 powder diffractometer with Bragg−Brentano geometry at a voltage of 44 kV and current of 40 mA with Cu−Kα radiation (λ = 1.5406 Å). PXRD was collected for all systems, both before and after thermal conditioning. All samples were finely ground in an argon-filled glovebox and packed into a zero-background sample holder covered with Kapton film to prevent exposure to humid air. Each measurement was collected from the 2θ range of 10°−80° with a step size of 0.03°.

Scanning Electron Microscopy (SEM) and Electron Dispersive X-ray Spectroscopy (EDX)

Scanning electron microscopy (SEM) coupled with energy-dispersive X-ray spectroscopy (EDX) was employed to examine the morphology and elemental distribution of the Li_3PO_4−LiI samples. Two pellets were prepared by pressing approximately 70 mg of the synthesized powder. One pellet was analyzed in the as-pressed condition (Pre-TC), while the second pellet was subjected to thermal conditioning before analysis (Post-TC). SEM imaging and EDX mapping of both samples were performed using a Thermo Fisher Helios G4 dual-beam FIB-SEM equipped with an Oxford Instruments EDX detector. Images were acquired at an accelerating voltage of 15 kV with a beam current of 0.4−0.8 nA.

Solid-State NMR

Samples were packed into 2.5 mm and 4 mm zirconia rotors with Vespel caps in an argon-filled glovebox. For all systems, ^{6}Li, ^{7}Li, and ^{31}P Magic-Angle Spinning (MAS) solid-state nuclear magnetic resonance (NMR) experiments were performed using a Bruker Avance-III 500 MHz (11.7 T) spectrometer at Larmor frequencies of 73.6 MHz, 194.4 MHz, and 202.4 MHz, respectively. All samples were spun at a MAS rate of 25 kHz using a 2.5 mm Bruker triple-resonance (HXY) probe. Single-pulse ^{6}Li MAS NMR experiments were performed with a $\pi/2$ pulse length of 6.70 μs and a recycle delay of 500 s for Li_3PO_4−LiI, 6.7 μs and 200 s for Li_3YBr_6, and 6.50 μs and 1000 s for Li_3PS_4. Single-pulse ^{7}Li MAS NMR experiments were performed with a $\pi/2$ pulse length of 3.2 μs and a recycle delay of 20 s for Li_3PO_4−LiI, 3.2 μs and 100 s for Li_3YBr_6, and 3.3 μs and 50 s for Li_3PS_4. ^{31}P MAS NMR experiments were performed with a $\pi/2$ pulse

https://doi.org/10.1021/acs.chemmater.5c03118
Chem. Mater. 2026, 38, 3383−3391

length of 4.0 μs and a recycle delay of 20 s for Li_3PS_4. NMR data were collected for samples both before and after thermal conditioning.

In-situ variable-temperature ^{7}Li MAS NMR measurements were conducted to probe ion dynamics and changes in local structures during thermal conditioning using a Bruker Avance-I 300 MHz (7.04 T) spectrometer at a Larmor frequency of 116.6 MHz. All samples were spun at a MAS rate of 10 kHz using a 4 mm Bruker triple-resonance HXY probe. The 1D NMR spectra were obtained using the single-pulse sequence with a $\pi/2$ pulse length of 3.1 μs and a recycle delay of 20 s for Li_3PO_4–LiI, 3.3 μs and 200 s for Li_3YBr_6, and 3.4 μs and 20 s for Li_3PS_4. The inversion recovery pulse sequence ($\pi - \pi/2$) was used to determine the ^{7}Li T_1 relaxation times between 25 and 100 °C. Once the temperature reached 100 °C, NMR measurements were performed from 100 to 25 °C. Room-temperature NMR experiments were performed before and after the VT-NMR experiments. Note that the temperature range for Li_3PS_4 was limited to 25–90 °C to prevent phase degradation.

The ^{6,7}Li NMR spectra were referenced to dry $LiCl_{(s)}$ at −1.1 ppm. The ^{31}P NMR spectra were referenced to 85% $H_3PO_{4(aq)}$ at 0 ppm.

^{6}Li NMR Calculations[33]

Geometry relaxation and NMR chemical shielding calculations using plane-wave density functional theory (DFT) were conducted with the Cambridge Serial Total Energy Package (CASTEP, v. 21.11),[34,35] which implements periodic boundary conditions within the pseudopotential approximation. The Perdew–Burke–Ernzerhof (PBE) exchange-correlation functional within the generalized-gradient approximation GGA[36] was employed. The plane-wave basis sets were truncated at a cutoff energy of 600 eV with a 2 × 4 × 4 k-point set and on-the-fly generated pseudopotentials. Atomic positions and lattice parameters were fully relaxed using the Limited-memory Broyden-Fletcher-Goldfarb-Shanno (LBFGS) optimize[37,38] until all forces were smaller than 0.1 eV/Å. For NMR chemical shielding calculations, a cutoff energy of 800 eV and a 2 × 4 × 4 k-point set utilizing on-the-fly generated pseudopotentials were employed.

RESULTS AND DISCUSSION

Thermal Conditioning of Solid Electrolytes for Enhanced Ionic Conductivity

Electrochemical impedance spectroscopy measurements were conducted to determine the ionic conductivity before and after thermal conditioning (TC). Pre-thermal conditioning (Pre-TC) refers to samples as-prepared without further heat treatment, as described in the Experimental Methods section. Post-thermal conditioning (Post-TC) refers to the process of exposing samples to a single slow heating cycle from room temperature to 100 °C, then cooling to 25 °C. Room-temperature ionic conductivities (σ_{RT}) of the three representative solid electrolytes pre- and post-TC are shown in Table 1. After TC, the ionic conductivities at room temperature for all the solid electrolytes increase by at least ∼40%. The glassy oxyhalide, Li_3PO_4–LiI shows the most significant improvement with an increase of 67% from 0.15 mS cm^{-1} to 0.25 mS cm^{-1}. The halide system (Li_3YBr_6) exhibits an improvement of 48% from 1.65 mS cm^{-1} to 2.45 mS cm^{-1}, and the sulfide system (Li_3PS_4) exhibits an improvement of 38%, from 0.47 mS cm^{-1} to 0.65 mS cm^{-1}. In addition, variable-temperature EIS measurements show that the activation energies for ion transport also decrease with TC (Figures 1 and S1). The equivalent circuit fittings of the EIS spectra for the three solid electrolytes, after thermal conditioning (25 °C, cooling), are provided in Figure S2.

Table 1. Effect of Thermal Conditioning (TC) on Ionic Conductivity (σ_{RT})[a]

	Conductivity [mS cm^{-1}]		
Material	Pre-TC	Post-TC	Relative Percent Increase [%]
Li_3PO_4–LiI	0.15	0.25	67
Li_3YBr_6	1.65	2.45	48
Li_3PS_4	0.47	0.65	38

[a]Conductivities of Li_3PO_4–LiI, Li_3YBr_6, and Li_3PS_4 at room temperature before and after thermal conditioning.

The Influence of Thermal Conditioning on Structures

To further understand the origin of the observed thermal conditioning-induced improvement in ion transport, powder X-ray diffraction (P-XRD) was used to examine changes in long-range structures and chemical phases in the systems before and after thermal conditioning (TC). The P-XRD of Li_3PO_4–LiI is shown in Figure 2a. The observed Bragg peaks correspond to crystalline LiI and LiI·H_2O. Rietveld refinement confirms that these residual crystalline phases account for all detectable long-range order in the sample (Figure S3).[13] The conductive phase, Li_4PO_4I, itself lacks a well-defined long-range structure and does not produce additional diffraction peaks, consistent with its amorphous or highly disordered nature. Recent work by Patel and coworkers has demonstrated that LiI improves electrochemical performance by reacting with Li_3PO_4 to form an interphase that facilitates Li^+-ion migration.[13] Prior AIMD simulations indicate that glassy Li_4PO_4I exhibits significantly enhanced Li^+ diffusivity (activation energy ∼ 0.37 eV) relative to crystalline Li_3PO_4I polymorphs, whereas ordered Li_4PO_4I is poorly conductive (Figure S4).[13] These insights suggest that the improvement in ionic conductivity for Li_3PO_4–LiI is due to more subtle, local structural changes. Therefore, other advanced characterization techniques are needed to support the enhanced ionic conductivity observed after TC.

The successful synthesis of Li_3YBr_6 was confirmed by P-XRD, as the diffraction pattern of the as-prepared sample shows excellent agreement with the pattern derived from the ICSD database (ICSD No. 29961, space group $C2/m$) (Figure 2b). After thermal conditioning, no additional crystalline phases are observed, indicating that TC does not induce bulk phase transformation. Instead, a decrease in residual LiBr impurity is evident, as indicated by the elimination of Bragg peaks at approximately 28.0°, 32.5°, and 55.0°. The removal of the residual LiBr is one of the explanations for the improvement in the overall ionic conductivity, because LiBr is known to be a poor Li^+-ion conductor.[39] Notably, the differences in peak intensities between pre- and post-TC for Li_3YBr_6 are due to the preferred orientation of the system.[33]

Lastly, Li_3PS_4 is predominantly amorphous before TC, whereas weak Bragg peaks that appear after TC indicate the formation of small crystallites. Rietveld refinement confirms this partial crystallization, supporting the classification of the thermally conditioned sample as a glass-ceramic electrolyte (Figures 2c, S5). No common impurities such as Li_2S and P_2S_5 are found (Figure S6). Additional characterization techniques are used to decipher the structure-dynamics correlation.

Structure-Ion Dynamics Correlation

To further investigate changes in structure and understand their correlation with ion transport properties, solid-state nuclear magnetic resonance (NMR) was employed. Variable-temperature ^{7}Li MAS NMR measurements were collected for all samples as they were heated from 25 to 100 °C and then

https://doi.org/10.1021/acs.chemmater.5c03118
Chem. Mater. 2026, 38, 3383–3391

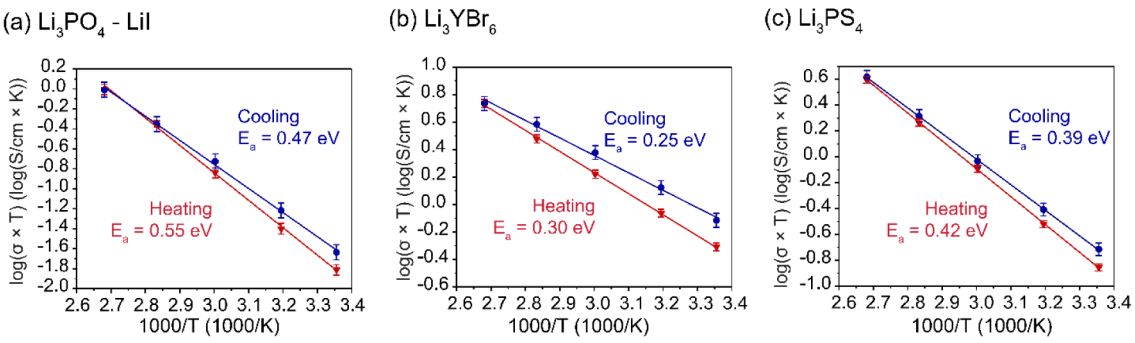

Figure 1. Effects of thermal conditioning on ion transport in exemplary oxyhalide-, halide-, and thiophosphate-based Li^+-ion conductors. Arrhenius plots of ionic conductivity versus temperature and the extracted activation energies (E_a) upon heating and cooling in Li_3PO_4–LiI (a), Li_3YBr_6 (b), and Li_3PS_4 (c).

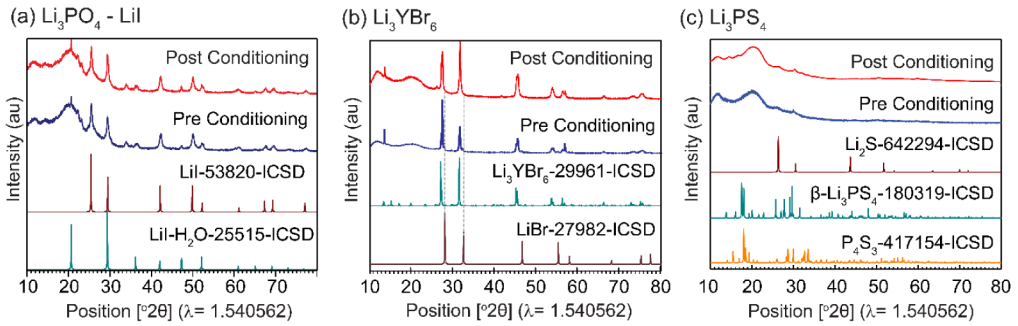

Figure 2. Changes in average structures of solid electrolytes pre- and post-thermal conditioning. P-XRD patterns of (a) Li_3PO_4–LiI, (b) Li_3YBr_6, and (c) Li_3PS_4 pre- and post-thermal conditioning. The XRD patterns of LiI (ICSD #53820), LiI–H_2O (ICSD #25515), LiBr (ICSD #27982), and Li_2S (ICSD #27982) are shown as references.

cooled to 25 °C in 20 °C increments. ^{7}Li is a spin-$^3/_2$ nucleus with corresponding NMR resonances composed of a central transition (CT, $+1/2 \leftrightarrow -1/2$) and satellite transitions (ST, $3/2 \leftrightarrow -1/2$, $1/2 \leftrightarrow -3/2$) due to the interactions of the quadrupole moment with electric field gradients (EFGs). However, fast Li^+ motion in ion conductors averages quadrupolar effects, so CT dominates. ^{7}Li–^{7}Li dipolar interactions are another major source of line broadening. The orientation dependence of both the quadrupolar and dipolar interactions can result in broad powder patterns,[40] which are narrowed by molecular motion at elevated temperatures or magic angle spinning (MAS). The central transition in all the systems of interest manifests as a Gaussian line shape both pre- and post-TC (Figure 3) in ^{7}Li NMR. Figure 3 also displays the in situ variable-temperature ^{7}Li MAS NMR spectra for the three classes of electrolytes. As the sample temperature increases (Figure 3a–c), the ^{7}Li MAS (10 kHz) NMR line widths of all phases in each system decrease significantly. Comparing the spectra acquired at 25 and 100 °C, the line width decreases from 310 to 280 Hz for Li_3PO_4–LiI, 160 to 130 Hz for Li_3YBr_6, and 90 to 80 Hz for Li_3PS_4. The narrowing effect in the ^{7}Li NMR arises from faster Li^+-ion hopping processes.[41,42] The comparison of ^{7}Li MAS (25 kHz) NMR spectra of pre- and post-TC samples (Figure 3d–f) shows that the line shape narrows by more than 10% after TC for both Li_3PO_4–LiI and Li_3YBr_6. The change in the ^{7}Li MAS NMR line width upon TC for Li_3PS_4 is small (from 20 to 19 Hz) and not statistically significant. Therefore, ^{31}P MAS NMR was employed to probe the origin of the enhanced ionic conductivity, which will be discussed later. The parameters for fitting the ^{7}Li MAS NMR spectra (Figure 3d–f) are listed in Table 2. In addition to decreased line widths, the peak positions also shift, indicating changes in local structures or chemical phases following TC. Therefore, high-resolution ^{6}Li MAS NMR is required to examine such subtle changes.

Due to the lower natural abundance of ^{6}Li (7.59% for ^{6}Li vs 92.41% for ^{7}Li), a smaller quadrupolar moment (−0.08 b for ^{6}Li vs −4.01 b for ^{7}Li), and a smaller magnetogyric ratio (+6.267 MHz/T for ^{6}Li vs +16.546 MHz/T for ^{7}Li), ^{6}Li MAS NMR often exhibits higher resolution compared with ^{7}Li MAS NMR, due to weaker quadrupolar and dipolar interactions. Therefore, ^{6}Li MAS NMR is used to examine changes in local structure and phase in greater detail. The comparison of the ^{6}Li MAS NMR spectra of Li_3PO_4–LiI (Figure 4a) pre- and post-TC reveals an additional resonance at ∼−1.5 ppm, assigned to Li-rich $Li_4PO_4I_4$ ($Li_{4+x}PO_4I_{4+x}$).[13] Patel and coworkers demonstrated that glassy Li_4PO_4I plays a crucial role in facilitating Li^+-ion migration within the material, acting as a favorable interphase to promote Li^+-ion hopping between Li_3PO_4 and LiI. ^{6}Li DFT NMR calculations from the same study confirm the presence of glassy Li_4PO_4I. The −0.7 ppm resonance lies at the weighted average between Li_3PO_4 (0.32 ppm) and LiI (−4.45 ppm), indicating that mobile Li^+ ions rapidly hop between PO_4^{3-} and I^- environments with no preferential trapping, consistent with fast Li^+ transport in the disordered phase (Figure S7).[13] Additionally, the ^{6}Li MAS NMR reveals that the LiI content decreases after TC. LiI is a known low-conducting material,[43] and the presence of LiI could lower the overall ionic conductivity of the Li_3PO_4–LiI material. As a result, the increase in the glassy Li_4PO_4I phase and the reduction of LiI after TC are attributed to the enhanced ionic conductivity. SEM and EDX analyses were

https://doi.org/10.1021/acs.chemmater.5c03118
Chem. Mater. 2026, 38, 3383−3391

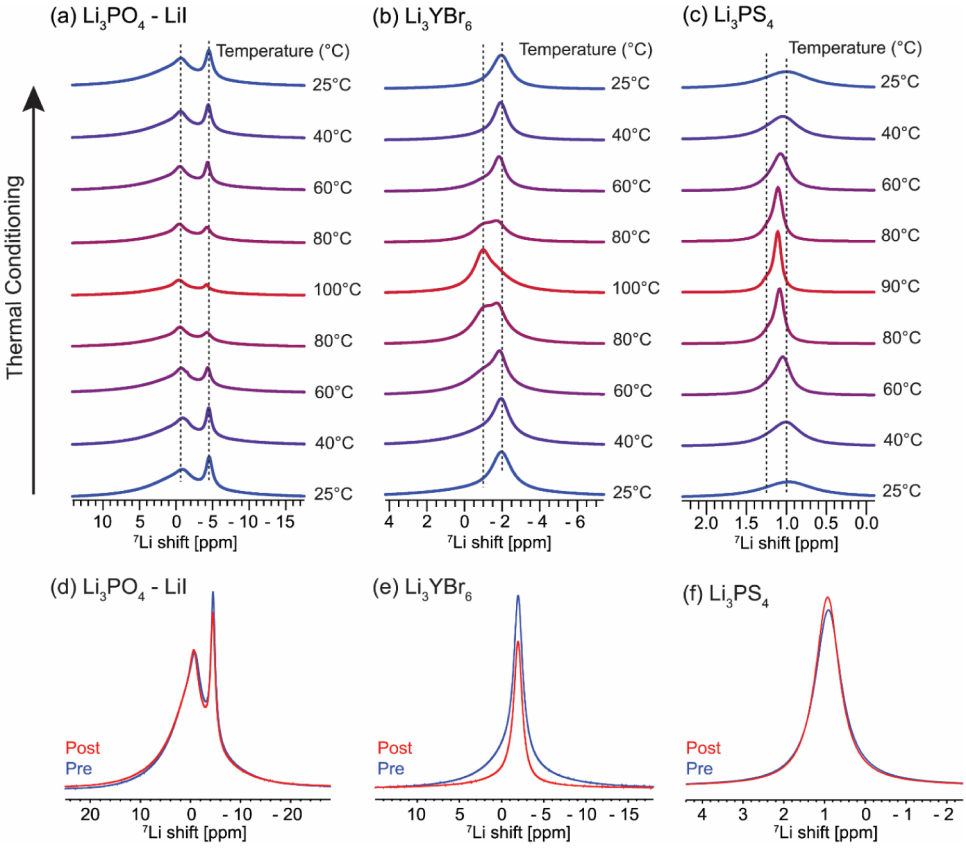

Figure 3. ^{7}Li MAS NMR to probe changes in local structures and ion dynamics for oxyhalide-, halide-, and thiophosphate-based Li^{+}-ion conductors. Variable-temperature ^{7}Li MAS NMR of Li_3PO_4–LiI from 25–100 °C (a), Li_3YBr_6 from 25–100 °C (b), and Li_3PS_4 from 25–90 °C (c), all measured with a MAS rate of 10 kHz. The room-temperature ^{7}Li MAS NMR spectra of Li_3PO_4–LiI (d), Li_3YBr_6 (e), and Li_3PS_4 (f) pre- and post-thermal conditioning measured with a MAS rate of 25 kHz.

Table 2. Effect of Thermal Conditioning Probed by ^{7}Li MAS NMR for Oxyhalide-, Halide-, and Thiophosphate-Based Li^{+}-ion Conductors[a]

	δ_{iso} (ppm)		Line Broadening (Hz)	
Material	Pre-TC	Post-TC	Pre-TC	Post-TC
Li_3PO_4–LiI	−0.82	−0.64	310	280
Li_3YBr_6	−1.92	−1.75	26	16
Li_3PS_4	1.38	1.28	20	19

[a] ^{7}Li MAS NMR parameters of Li_3PO_4–LiI, Li_3YBr_6, and Li_3PS_4 at room temperature pre- and post-thermal conditioning.

performed to investigate the microstructural and compositional evolution of the Li_3PO_4–LiI samples. In contrast to the pre-TC sample, the post-TC SEM image revealed more compacted grains and enhanced interparticle necking, indicating improved particle connectivity and reduced microstructural heterogeneity (Figure S8). Additionally, the EDX mapping showed that the iodine distribution, initially heterogeneous and segregated from the PO_4^{3-} in the pre-TC sample, becomes significantly more uniform after TC, suggesting incorporation of LiI into Li_3PO_4 to form the more conductive Li_4PO_4I phase (Figure S9). These observations provide direct evidence of the evolution of phase inhomogeneities and support the proposed impurity removal in Li_3PO_4–LiI after TC.

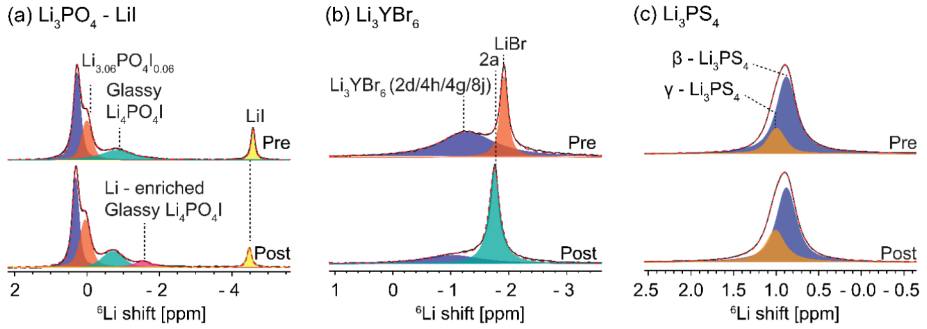

Figure 4. ^{6}Li MAS NMR to probe local structure for oxide-, halide-, and thiophosphate-based Li^{+}-ion conductors. ^{6}Li NMR spectra of Li_3PO_4–LiI (a), Li_3YBr_6 (b), and Li_3PS_4 (c) pre- and post-thermal conditioning.

https://doi.org/10.1021/acs.chemmater.5c03118
Chem. Mater. 2026, 38, 3383−3391

The Li_3YBr_6 case also exhibits a reduced amount of the nonconductive phase, i.e., LiBr, after TC, and is accompanied by more subtle and interesting changes. Li in Li_3YBr_6 can reside in 5 Wyckoff sites, 2d/4h/4g/8j/2a. ^{6}Li MAS NMR resolves the Li sites contributing to ion migration (2d/4h/4g/8j) and the less mobile site (2a).[9,33] ^{6}Li NMR calculations were also performed to assist with the site assignments, and the results are provided in Table S1.[33] Before TC, the Li sites contributing to Li^+-ion migration (i.e., 2d/4h/4g/8j) manifest as a single peak at approximately −1.2 ppm in ^{6}Li MAS NMR (Figure 4b), due to rapid Li^+ hopping among these sites. The sharp peak at approximately −2.0 ppm corresponds to the LiBr impurity, as confirmed by X-ray diffraction. After TC, a downfield shift with larger ppm values is observed for both the broad and sharp resonances. The downfield shift from −2.0 ppm to −1.8 ppm indicates the removal of LiBr, as seen from P-XRD. The resonance at −1.8 ppm is attributed to the Li_{2a} of Li_3YBr_6, as confirmed by DFT NMR calculations.[33] The slight downfield shift of the 2d/4h/4g/8j resonance indicates a redistribution of Li^+ among the 2d/4h/4g/8j sites in Li_3YBr_6 while undergoing TC, and the intensity loss is likely due to Li^+ hopping rate falling into the intermediate motional regime, which significantly broadens the coalesced resonance.[44] This is consistent with the variable-temperature ^{7}Li MAS NMR, where the coalesced resonance sharpens significantly at elevated temperatures, overshadowing the Li_{2a}/LiBr peak (Figure 3b). Therefore, the impact of TC on Li_3YBr_6 is the elimination of LiBr impurities and the redistribution of Li^+ ions. From our prior studies, Li^+ redistribution often leads to increased Li^+ occupancy at the 2d/4h/4g/8j sites responsible for long-range ion conduction.[33] A schematic illustration of the Li^+ redistribution and local structural rearrangements in Li_3YBr_6 is provided in Figure S10.

The ^{6}Li MAS NMR of Li_3PS_4 reveals no significant changes, and the Li_3PS_4 remains predominantly β-Li_3PS_4 (Figure 4c). As a result, ^{31}P NMR was also collected to understand the changes in Li_3PS_4 further. The resulting fitting parameters (chemical shift, line width, and integral) are provided in Table S2. The ^{31}P MAS NMR of the pre-TC sample reveals two resonances at 86.7 and 107.2 ppm, assigned to isolated $(PS_4)^{3-}$ tetrahedra and $(P_2S_6)^{4-}$ units, respectively (Figure 5). Similar to the ^{7}Li NMR, the peak width also narrows post-TC for ^{31}P NMR. The sample remains predominantly amorphous, as indicated by the broad peaks. In addition, the $(P_2S_6)^{4-}$ resonance at 107.2 ppm disappears, and is replaced by the $(P_2S_7)^{4-}$ resonance at 105.0 ppm. $(P_2S_7)^{4-}$ generally promotes higher Li^+ ionic conductivity compared to $(P_2S_6)^{4-}$;

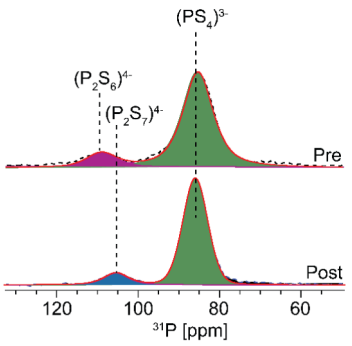

Figure 5. ^{31}P MAS NMR spectra of Li_3PS_4 pre- and post-thermal conditioning, with assignments of ^{31}P resonances.

thiophosphates, such as the $Li_7P_3S_{11}$, containing mixed polyanions of $(P_2S_7)^{4-}$ and $(PS_4)^{3-}$, are among the best Li^+ solid electrolytes.[45,46] Therefore, the $(P_2S_6)^{4-} \rightarrow (P_2S_7)^{4-}$ transition in Li_3PS_4 post-TC facilitates faster Li^+ ion conduction.

Moreover, ^{7}Li MAS NMR T_1 relaxation times were measured to probe Li^+-ion dynamics. According to the Bloembergen, Purcell, and Pound (BPP) model, the T_1 relaxation time is a function of motional rate $(1/\tau_c)$, as shown in eq 1:

$$\left(\frac{1}{T_1}\right) = \frac{3\mu_o^2\gamma^4\hbar^2}{10r_o^6}\left[\frac{\tau_c}{1+(\omega_o\tau_c)^2} + \frac{4\tau_c}{1+4(\omega_o\tau_c)^2}\right] \quad (1)$$

Where μ_o is the vacuum permeability, γ is the gyromagnetic ratio, $\hbar$ is the reduced Planck constant, r_o is the interatomic distance, and ω_o is the Larmor frequency. In the slow-motion regime ($\omega_o\tau_c \gg 1$; ω_o = 116.64 MHz), T_1 decreases with increasing motional rate. In the fast-motion regime ($\omega_o\tau_c \ll 1$; ω_o = 116.64 MHz), T_1 increases with increasing motional rate.[47−49] To determine if the T_1 values lie in the slow- or fast-motion regime, variable-temperature ^{7}Li NMR T_1 relaxation times were determined for the three systems (Figure 6). For all three solid electrolytes, the T_1 values decrease with increasing temperature, indicating Li^+-ion motion in this material lies in the slow-motion regime of the BPP model. Therefore, a shorter T_1 relaxation time indicates faster ion motion.[48]

The average T_1 relaxation time for all the phases in Li_3PO_4−LiI decreases after TC from 3.16 to 2.21 s (Figure 6a). The ^{7}Li T_1 values for all phases in Li_3PO_4−LiI were confirmed to decrease with TC (Figure S11), and individual T_1 values for each phase are provided in Table S3. Among them, $Li_{4+x}PO_4I_{1+x}$ exhibits the shortest T_1 and the largest T_1 reduction post-TC, suggesting the fastest Li^+ conduction. Therefore, TC increases the fraction of more conductive phases and enhances ion mobility in all phases, collectively resulting in higher ionic conductivity.

As for the Li_3YBr_6 system, a slight increase in the ^{7}Li T_1 NMR relaxation times is observed (Figure 6b), suggesting relatively slower local Li^+ dynamics. The overall improvement in ionic conductivity is likely due to the redistribution of Li^+ to higher-mobility sites and the removal of LiBr impurities. The sizable decrease in activation energy from 0.30 to 0.25 eV also suggests modifications to ion transport pathways, likely induced by Li^+ redistribution.

Similarly, for Li_3PS_4, the T_1 relaxation time does not change significantly with TC (Figure 6c). The T_1 decreases from 1.35 to 1.32 s before and after TC. It is not surprising, as the local Li^+ mobility is mainly determined by Li^+−PS_4^{3-} interactions, which are largely unchanged. The impartment of a small fraction of P_2S_7 units possibly modifies the global energy landscape and leads to a lower activation energy, rather than affecting local ion mobility.

CONCLUSION

Thermal conditioning is a promising strategy for improving ionic conductivity in oxyhalide, halide, and thiophosphate solid electrolytes. The slow heat−cool cycles at moderate temperatures can enhance performance by nearly 40% for all the solid-electrolyte systems examined. Multimodal characterizations revealed several underlying mechanisms: (1) the removal of low-conductivity impurities and the generation of high-conductivity phases, (2) redistribution of active cations, (3)

https://doi.org/10.1021/acs.chemmater.5c03118
Chem. Mater. 2026, 38, 3383−3391

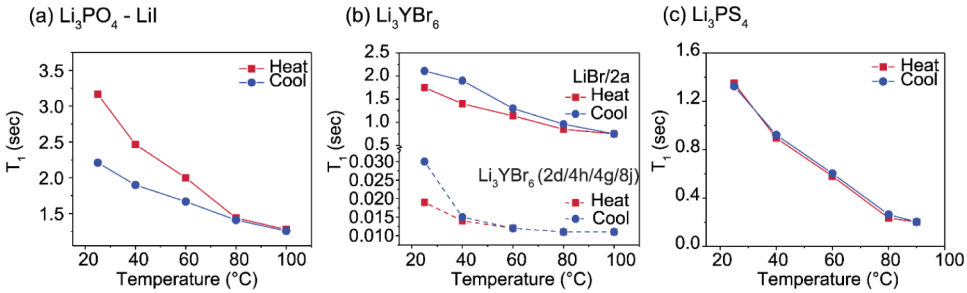

Figure 6. Effect of thermal conditioning on solid electrolytes probed by NMR T_1 relaxation measurements. Variable-temperature ^{7}Li NMR T_1 relaxation time measurements of Li_3PO_4–LiI (a), Li_3YBr_6 (b), and Li_3PS_4 (c). As Li^+-ion mobility increases with temperature, the measurements suggest that shorter T_1 values correlate with faster Li^+-ion motion in the temperature ranges of 25–100 °C for Li_3PO_4–LiI and Li_3YBr_6, and 25–90 °C for Li_3PS_4.

modification of the anion sublattice to induce disorder conducive for fast ion conduction, and (4) increased ion mobility. Overall, this work presents a practical and generally applicable approach for enhancing ion transport in glass-ceramic electrolytes at low cost, and elucidates the subtle yet essential structural and dynamical changes that lead to performance enhancement.

■ ASSOCIATED CONTENT

Supporting Information

The Supporting Information is available free of charge at https://pubs.acs.org/doi/10.1021/acs.chemmater.5c03118.

Nyquist plots of the electrochemical impedance spectroscopy measurements for Li_3PO_4–LiI, Li_3YBr_6, and Li_3PS_4 across temperature; equivalent circuit fitting of impedance spectra; Rietveld refinements and powder X-ray diffraction analysis; Li^+ diffusion and diffusivity calculations; DFT ^{6}Li NMR calculations; SEM micrographs and EDX elemental mapping; schematic illustration of Li^+ redistribution and local structural rearrangements; ^{7}Li MAS NMR spectra and relaxation measurements; calculated ^{6}Li NMR shifts; NMR parameters for ^{31}P resonances in Li_3PS_4; and ^{7}Li relaxation times for Li_3PO_4–LiI phases before and after thermal conditioning (PDF)

■ AUTHOR INFORMATION

Corresponding Author

Yan-Yan Hu – *Department of Chemistry and Biochemistry, Florida State University, Tallahassee, Florida 32306, United States; Center of Interdisciplinary Magnetic Resonance, National High Magnetic Field Laboratory, Tallahassee, Florida 32310, United States;* orcid.org/0000-0003-0677-5897; Email: yhu@fsu.edu

Authors

Islamiyat Ojelade – *Department of Chemistry and Biochemistry, Florida State University, Tallahassee, Florida 32306, United States; Center of Interdisciplinary Magnetic Resonance, National High Magnetic Field Laboratory, Tallahassee, Florida 32310, United States*

Erica Truong – *Department of Chemistry and Biochemistry, Florida State University, Tallahassee, Florida 32306, United States; Center of Interdisciplinary Magnetic Resonance, National High Magnetic Field Laboratory, Tallahassee, Florida 32310, United States*

Tej P. Poudel – *Department of Chemistry and Biochemistry, Florida State University, Tallahassee, Florida 32306, United States; Center of Interdisciplinary Magnetic Resonance, National High Magnetic Field Laboratory, Tallahassee, Florida 32310, United States; Materials Science and Engineering Program, Florida State University, Tallahassee, Florida 32310, United States*

Sawankumar Patel – *Department of Chemistry and Biochemistry, Florida State University, Tallahassee, Florida 32306, United States; Center of Interdisciplinary Magnetic Resonance, National High Magnetic Field Laboratory, Tallahassee, Florida 32310, United States*

Pawan K. Ojha – *Department of Chemistry and Biochemistry, Florida State University, Tallahassee, Florida 32306, United States; Center of Interdisciplinary Magnetic Resonance, National High Magnetic Field Laboratory, Tallahassee, Florida 32310, United States*

Yudan Chen – *Department of Chemistry and Biochemistry, Florida State University, Tallahassee, Florida 32306, United States; Center of Interdisciplinary Magnetic Resonance, National High Magnetic Field Laboratory, Tallahassee, Florida 32310, United States*

Ifeoluwa Oyekunle – *Department of Chemistry and Biochemistry, Florida State University, Tallahassee, Florida 32306, United States; Center of Interdisciplinary Magnetic Resonance, National High Magnetic Field Laboratory, Tallahassee, Florida 32310, United States*

Yongkang Jin – *Department of Chemistry and Biochemistry, Florida State University, Tallahassee, Florida 32306, United States; Center of Interdisciplinary Magnetic Resonance, National High Magnetic Field Laboratory, Tallahassee, Florida 32310, United States*

Md Mahinur Islam – *Department of Chemistry and Biochemistry, Florida State University, Tallahassee, Florida 32306, United States; Center of Interdisciplinary Magnetic Resonance, National High Magnetic Field Laboratory, Tallahassee, Florida 32310, United States*

Tehreem Toheed – *Department of Chemistry and Biochemistry, Florida State University, Tallahassee, Florida 32306, United States; Center of Interdisciplinary Magnetic Resonance, National High Magnetic Field Laboratory, Tallahassee, Florida 32310, United States*

Hannah Matos-Pimentel – *Center of Interdisciplinary Magnetic Resonance, National High Magnetic Field Laboratory, Tallahassee, Florida 32310, United States*

Joey Peterson – *Department of Chemistry and Biochemistry, Florida State University, Tallahassee, Florida 32306, United*

States; Center of Interdisciplinary Magnetic Resonance, National High Magnetic Field Laboratory, Tallahassee, Florida 32310, United States; orcid.org/0009-0000-7473-6967

Complete contact information is available at: https://pubs.acs.org/10.1021/acs.chemmater.5c03118

Author Contributions

‖I.O., E.T., and T.P.P. contributed equally to this work.

Notes

The authors declare no competing financial interest.

■ ACKNOWLEDGMENTS

The authors acknowledge the support from the National Science Foundation under grant no. DMR-2319151. All solid-state NMR and SEM-EDX experiments were performed at the National High Magnetic Field Laboratory by the National Science Foundation Cooperative agreement Nos. DMR-1644779 and DMR-2128556, and the State of Florida.

■ REFERENCES

(1) Goodenough, J. B.; Park, K.-S. The Li-Ion Rechargeable Battery: A Perspective. *J. Am. Chem. Soc.* **2013**, *135* (4), 1167−1176.
(2) Zhang, D.; Xu, X.; Qin, Y.; Ji, S.; Huo, Y.; Wang, Z.; Liu, Z.; Shen, J.; Liu, J. Recent Progress in Organic−Inorganic Composite Solid Electrolytes for All-Solid-State Lithium Batteries. *Chem. - Eur. J.* **2020**, *26* (8), 1720−1736.
(3) Alkhedher, M.; Al Tahhan, A. B.; Yousaf, J.; Ghazal, M.; Shahbazian-Yassar, R.; Ramadan, M. Electrochemical and Thermal Modeling of Lithium-Ion Batteries: A Review of Coupled Approaches for Improved Thermal Performance and Safety Lithium-Ion Batteries. *J. Energy Storage* **2024**, *86*, 111172.
(4) Andriunas, I.; Milojevic, Z.; Wade, N.; Das, P. K. Impact of Solid-Electrolyte Interphase Layer Thickness on Lithium-Ion Battery Cell Surface Temperature. *J. Power Sources* **2022**, *525*, 231126.
(5) Ahmad, H.; Kubra, K. T.; Butt, A.; Nisar, U.; Iftikhar, F. J.; Ali, G. Recent Progress, Challenges, and Perspectives in the Development of Solid-State Electrolytes for Sodium Batteries. *J. Power Sources* **2023**, *581*, 233518.
(6) Hou, M.; Liang, F.; Chen, K.; Dai, Y.; Xue, D. Challenges and Perspectives of NASICON-Type Solid Electrolytes for All-Solid-State Lithium Batteries. *Nanotechnology* **2020**, *31* (13), 132003.
(7) Luo, X.; Zhong, Y.; Wang, X.; Xia, X.; Gu, C.; Tu, J. Ionic Conductivity Enhancement of Li_2 $ZrCl_6$ Halide Electrolytes via Mechanochemical Synthesis for All-Solid-State Lithium−Metal Batteries. *ACS Appl. Mater. Interfaces* **2022**, *14* (44), 49839−49846.
(8) Schlem, R.; Banik, A.; Ohno, S.; Suard, E.; Zeier, W. G. Insights into the Lithium Sub-Structure of Superionic Conductors Li_3 YCl_6 and Li_3 YBr_6. *Chem. Mater.* **2021**, *33* (1), 327−337.
(9) Gombotz, M.; Wilkening, H. M. R. Fast Li Ion Dynamics in the Mechanosynthesized Nanostructured Form of the Solid Electrolyte Li_3 YBr_6. *ACS Sustainable Chem. Eng.* **2021**, *9* (2), 743−755.
(10) Homma, K.; Yonemura, M.; Kobayashi, T.; Nagao, M.; Hirayama, M.; Kanno, R. Crystal Structure and Phase Transitions of the Lithium Ionic Conductor Li3PS4. *Solid State Ionics* **2011**, *182* (1), 53−58.
(11) Hofer, M.; Grube, M.; Burmeister, C. F.; Michalowski, P.; Zellmer, S.; Kwade, A. Effective Mechanochemical Synthesis of Sulfide Solid Electrolyte Li3PS4 in a High Energy Ball Mill by Process Investigation. *Adv. Powder Technol.* **2023**, *34* (6), 104004.
(12) Kanazawa, K.; Yubuchi, S.; Hotehama, C.; Otoyama, M.; Shimono, S.; Ishibashi, H.; Kubota, Y.; Sakuda, A.; Hayashi, A.; Tatsumisago, M. Mechanochemical Synthesis and Characterization of Metastable Hexagonal Li_4 SnS_4 Solid Electrolyte. *Inorg. Chem.* **2018**, *57* (16), 9925−9930.
(13) Patel, S. V.; Truong, E.; Liu, H.; Jin, Y.; Chen, B. L.; Wang, Y.; Miara, L.; Kim, R.; Hu, Y.-Y. Interrupted Anion-Network Enhanced Li ± Ion Conduction in Li3+yPO4Iy. *Energy Storage Mater.* **2022**, *51*, 88−96.
(14) Yu, C.; Li, Y.; Adair, K. R.; Li, W.; Goubitz, K.; Zhao, Y.; Willans, M. J.; Thijs, M. A.; Wang, C.; Zhao, F.; Sun, Q.; Deng, S.; Liang, J.; Li, X.; Li, R.; Sham, T.-K.; Huang, H.; Lu, S.; Zhao, S.; Zhang, L.; Van Eijck, L.; Huang, Y.; Sun, X. Tuning Ionic Conductivity and Electrode Compatibility of Li3YBr6 for High-Performance All Solid-State Li Batteries. *Nano Energy* **2020**, *77*, 105097.
(15) Shimizu, K.; Bahuguna, P.; Mori, S.; Hayashi, A.; Watanabe, S. Enhanced Ionic Conductivity Through Crystallization of Li_3 PS_4 Glass by Machine Learning Molecular Dynamics Simulations. *J. Phys. Chem. C* **2024**, *128* (24), 10139−10145.
(16) Kaus, N. H.; Ahmad, A. H. Conductivity Studies and Ion Transport Mechanism in LiI−Li3PO4 Solid Electrolyte. *Ionics* **2009**, *15* (2), 197−201.
(17) Stöffler, H.; Zinkevich, T.; Yavuz, M.; Hansen, A.-L.; Knapp, M.; Bednarčík, J.; Randau, S.; Richter, F. H.; Janek, J.; Ehrenberg, H.; Indris, S. Amorphous versus Crystalline Li_3 PS_4: Local Structural Changes during Synthesis and Li Ion Mobility. *J. Phys. Chem. C* **2019**, *123* (16), 10280−10290.
(18) Wu, J.; Li, J.; Yao, X. Exploring the Potential of Halide Electrolytes for Next-Generation All-Solid-State Lithium Batteries. *Adv. Funct. Mater.* **2025**, *35* (10), 2416671.
(19) Liu, H.; Liu, Y.; Jing, S.; Hu, Y.; Zhang, Z.; Liu, S.; Liu, Y.; Zhuang, Z.; Li, F.; Liu, F. High-Performance Li3YCl3Br3 Halide Solid Electrolyte Synthesized Using Wet-Chemistry Route for All-Solid-State Battery. *Trans. Nonferrous Met. Soc. China* **2025**, *35* (7), 2341−2353.
(20) Deck, M. J.; Chien, P.; Poudel, T. P.; Jin, Y.; Liu, H.; Hu, Y. Oxygen-Induced Structural Disruption for Improved Li^+ Transport and Electrochemical Stability of Li_3 PS_4. *Adv. Energy Mater.* **2024**, *14* (4), 2302785.
(21) Banerjee, S.; Holekevi Chandrappa, M. L.; Ong, S. P. Role of Critical Oxygen Concentration in the β-Li_3 PS 4− x O $_x$ Solid Electrolyte. *ACS Appl. Energy Mater.* **2022**, *5* (1), 35−41.
(22) Asano, T.; Sakai, A.; Ouchi, S.; Sakaida, M.; Miyazaki, A.; Hasegawa, S. Solid Halide Electrolytes with High Lithium-Ion Conductivity for Application in 4 V Class Bulk-Type All-Solid-State Batteries. *Adv. Mater.* **2018**, *30* (44), 1803075.
(23) Poudel, T. P.; Deck, M. J.; Wang, P.; Hu, Y. Transforming Li_3 PS_4 Via Halide Incorporation: A Path to Improved Ionic Conductivity and Stability in All-Solid-State Batteries. *Adv. Funct. Mater.* **2024**, *34* (4), 2309656.
(24) Zeng, S.; Ding, X.; He, L.; Li, H.-W.; Zhang, Q.; Li, Y. Realizing Fast Li-Ion Conduction of Li_3 PO_4 Solid Electrolyte at Low Temperature by Mechanochemical Formation of Lithium-Containing Dual-Shells. *Mater. Adv.* **2023**, *4* (13), 2780−2784.
(25) Zakariyaou, S. Y.; Ye, H.; Jiang, C. Synthesis and Characterization of Lithium Phosphate (Li3PO4) as a Solid Electrolyte. *Batteries* **2024**, *10* (12), 429.
(26) Kong, L.; Li, Y.; Feng, W. Strategies to Solve Lithium Battery Thermal Runaway: From Mechanism to Modification. *Electrochem. Energy Rev.* **2021**, *4* (4), 633−679.
(27) Han, X.; Xu, Y.; Li, H.; Wang, Z.; Yue, J.; Yan, X.; Zhang, S.; Fu, J.; Xia, Y.; Zhou, L.; Wei, S.; Liu, X.; Wang, X.; Zhao, C.; Li, X.; Bo, S.-H.; Wang, J.; Sun, X.; Liang, J. Mechanically Robust Halide Electrolytes for High-Performance All-Solid-State Batteries. *Nat. Commun.* **2025**, *16* (1), 9770.
(28) Dubarry, M.; Qin, N.; Brooker, P. Calendar Aging of Commercial Li-Ion Cells of Different Chemistries − A Review. *Curr. Opin. Electrochem.* **2018**, *9*, 106−113.
(29) Hou, W.; Guo, X.; Shen, X.; Amine, K.; Yu, H.; Lu, J. Solid Electrolytes and Interfaces in All-Solid-State Sodium Batteries: Progress and Perspective. *Nano Energy* **2018**, *52*, 279−291.
(30) LePage, W. S.; Chen, Y.; Kazyak, E.; Chen, K.-H.; Sanchez, A. J.; Poli, A.; Arruda, E. M.; Thouless, M. D.; Dasgupta, N. P. Lithium

Mechanics: Roles of Strain Rate and Temperature and Implications for Lithium Metal Batteries. *J. Electrochem. Soc.* **2019**, *166* (2), A89.
(31) Wood, K. N.; Kazyak, E.; Chadwick, A. F.; Chen, K.-H.; Zhang, J.-G.; Thornton, K.; Dasgupta, N. P. Dendrites and Pits: Untangling the Complex Behavior of Lithium Metal Anodes through Operando Video Microscopy. *ACS Cent. Sci.* **2026**, *2*, 790−801.
(32) Feng, X.; Ouyang, M.; Liu, X.; Lu, L.; Xia, Y.; He, X. Thermal Runaway Mechanism of Lithium Ion Battery for Electric Vehicles: A Review. *Energy Storage Mater.* **2018**, *10*, 246−267.
(33) Poudel, T. P.; Truong, E.; Oyekunle, I. P.; Deck, M. J.; Ogbolu, B.; Chen, Y.; Ojha, P. K.; Gamaralalage, T. N. D. D.; Patel, S. V.; Jin, Y.; Hou, D.; Huang, C.; Li, T.; Liu, Y.; Xiong, H.; Hu, Y.-Y. Sliceable, Moldable, and Highly Conductive Electrolytes for All-Solid-State Batteries. *ACS Energy Lett.* **2025**, *10* (1), 40−47.
(34) Clark, S. J.; Segall, M. D.; Pickard, C. J.; Hasnip, P. J.; Probert, M. I. J.; Refson, K.; Payne, M. C. First Principles Methods Using CASTEP. *Z. Kristallogr. -Cryst. Mater.* **2005**, *220* (5−6), 567−570.
(35) Segall, M. D.; Lindan, P. J. D.; Probert, M. J.; Pickard, C. J.; Hasnip, P. J.; Clark, S. J.; Payne, M. C. First-Principles Simulation: Ideas, Illustrations and the CASTEP Code. *J. Phys.: condens. Matter.* **2002**, *14* (11), 2717.
(36) Perdew, J. P.; Burke, K.; Ernzerhof, M. Generalized Gradient Approximation Made Simple. *Phys. Rev. Lett.* **1996**, *77* (18), 3865−3868.
(37) Liu, D. C.; Nocedal, J. On the Limited Memory BFGS Method for Large Scale Optimization. *Math. Program.* **1989**, *45* (1), 503−528.
(38) Nocedal, J. Updating quasi-Newton matrices with limited storage. *Math. Comp.* **1980**, *35* (151), 773−782.
(39) Nakamura, O.; Goodenough, J. B. Conductivity Enhancement of Lithium Bromide Monohydrate by Al203 Particles. *Solid State Ionics* **1982**, *7* (4), 119−123.
(40) Chubak, I.; Alon, L.; Silletta, E. V.; Madelin, G.; Jerschow, A.; Rotenberg, B. Quadrupolar 23Na+ NMR Relaxation as a Probe of Subpicosecond Collective Dynamics in Aqueous Electrolyte Solutions. *Nat. Commun.* **2023**, *14* (1), 84.
(41) Song, A.; Turcheniuk, K.; Leisen, J.; Xiao, Y.; Meda, L.; Borodin, O.; Yushin, G. Understanding Li-Ion Dynamics in Lithium Hydroxychloride (Li_2 OHCl) Solid State Electrolyte via Addressing the Role of Protons. *Adv. Energy Mater.* **2020**, *10* (8), 1903480.
(42) Stöffler, H.; Zinkevich, T.; Yavuz, M.; Senyshyn, A.; Kulisch, J.; Hartmann, P.; Adermann, T.; Randau, S.; Richter, F. H.; Janek, J.; Indris, S.; Ehrenberg, H. Li^+ -Ion Dynamics in β-Li_3 PS_4 Observed by NMR: Local Hopping and Long-Range Transport. *J. Phys. Chem. C* **2018**, *122* (28), 15954−15965.
(43) Poulsen, F. Ionic Conductivity of Solid Lithium Iodide and Its Monohydrate. *Solid State Ionics* **1981**, *2* (1), 53−57.
(44) Hogrefe, K.; Minafra, N.; Zeier, W. G.; Wilkening, H. M. R. Tracking Ions the Direct Way: Long-Range Li^+ Dynamics in the Thio-LISICON Family Li_4 MCh_4 (M = Sn, Ge; Ch = S, Se) as Probed by ^{7}Li NMR Relaxometry and ^{7}Li Spin-Alignment Echo NMR. *J. Phys. Chem. C* **2021**, *125* (4), 2306−2317.
(45) Zhou, J.; Chen, P.; Wang, W.; Zhang, X. Li7P3S11 Electrolyte for All-Solid-State Lithium-Ion Batteries: Structure, Synthesis, and Applications. *Chem. Eng. J.* **2022**, *446*, 137041.
(46) Faizal, A.; Song, J. H.; Mercy, T. D.; Kim, D. K.; Kamala Bharathi, K. Improved Ionic Conductivity and Li7P3S11 Solid Electrolyte Based All-Solid State Batteries for Practical Applications. *J. Mater. Sci.: Mater. Electron.* **2024**, *35* (11), 749.
(47) Kuhn, A.; Kunze, M.; Sreeraj, P.; Wiemhöfer, H.-D.; Thangadurai, V.; Wilkening, M.; Heitjans, P. NMR Relaxometry as a Versatile Tool to Study Li Ion Dynamics in Potential Battery Materials. *Solid State Nucl. Magn. Reson.* **2012**, *42*, 2−8.
(48) Bloembergen, N.; Purcell, E. M.; Pound, R. V. Relaxation Effects in Nuclear Magnetic Resonance Absorption. *Phys. Rev.* **1948**, *73* (7), 679−712.
(49) Amanchukwu, C. V.; Gunnarsdottir, A. B.; Choudhury, S.; Newlove, T. L.; Magusin, P. C.; Bao, Z.; Grey, C. P. Understanding Lithium-Ion Dynamics in Single-Ion and Salt-in-Polymer Perfluoropolyethers and Polyethyleneglycol Electrolytes Using Solid-State NMR. *Macromeolecules* **2023**, *56* (10), 3650−3659.

https://doi.org/10.1021/acs.chemmater.5c03118
Chem. Mater. 2026, 38, 3383−3391